applied optics

GADICON spectrometer for ionosphere far-ultraviolet observation: prototype design, manufacturing, and testing

Lei Yu

Changchun Institute of Optics, Fine Mechanics and Physics, Chinese Academy of Sciences, Changchun 130033, China (top1gods@mail.ustc.edu.cn)

Received 27 June 2016; revised 27 July 2016; accepted 28 July 2016; posted 28 July 2016 (Doc. ID 269366); published 17 August 2016

The design, manufacturing, and testing of an imaging spectrometer prototype that will address new scientific requirements by the observation of the lower atmosphere's impact on the ionosphere are presented. The two sided lateral limb observation covering 130–180 nm far-ultraviolet (FUV) region allows the instrument to perform particle measurements in the daytime and nighttime. In this paper, we focus upon the working design principle, observation, and calibration.

OCIS codes: (120.4820) Optical systems; (120.6200) Spectrometers and spectroscopic instrumentation; (300.6190) Spectrometers; (300.6540) Spectroscopy, ultraviolet.

http://dx.doi.org/10.1364/AO.55.006662

1. INTRODUCTION

Satellite observations on far-ultraviolet-extreme-ultraviolet (FUV-EUV) radiation allow us to monitor the global characteristics of ionosphere content [1]. Continuous observations have been carried out since the 1980s [2]. Auroral Ionospheric Remote Sensor (AIRS), launched in 1986, provides three independent operational modes, including imaging, photometer, and spectrometer [3,4]. On the basis of development of 2D detector and the FUV optical layer techniques, the imaging spectrometer has been widely applied to the ionosphere observation in the 1990s: special sensor ultraviolet limb imager (SSULI) and special sensor ultraviolet spectrographic imager (SSUSI) for the U. S. Air Force defense meteorological satellite program (DMSP), and global ultraviolet imager (GUVI) for the thermosphere ionosphere mesosphere energetics and dynamics mission (TIMED) [5–10]. These instruments provide daily general coverage of the ionosphere in lateral limb and nadir observations, delivering different kinds of particle data in real time. It contributes significant data to the understanding of the state variables, energy, and dynamics of the mesosphere, lower thermosphere, and ionosphere.

These previous studies have proved that the ionosphere is the densest plasma between the Earth and Sun, and is traditionally held to be mainly influenced by forcing from above (solar radiation, solar wind/magnetosphere). However, some problems in space physics remain unresolved. For example [11–19]: (1) The daytime ionosphere exhibits significant variability in its motion and density, and the source of these changes has never been determined. (2) The ionosphere at low and middle latitudes suffers extreme changes during even moderate magnetic storms, and observations often depart greatly from predictions. (3) To understand the large variance, the observed changes of neutral and charged species must be evaluated together with the external drivers (from both above and below).

These problems are appearing with further research and are beginning to influence previous scientific identification. A key discovery of the last decade is that the ionosphere is strongly influenced by forces acting from below.

The following drivers should be measured by scientific instruments on satellites to resolve these scientific questions: neutral composition and winds in the thermosphere, along with the responses as electric field, plasma motion, and plasma density in the ionosphere. To continue to make progress, it is insufficient to make isolated measurements and images of parameters in the system. Rather, these observations of the drivers and the responses should be in a coordinated manner, at the same place and at the same time. The ultimate purpose is to understand the ion production, electric field, and wind forces resulting in the plasma distribution.

To implement the above measurements, a combination of different instruments is needed. The neutral wind profiler instrument, the neutral composition profiler instrument, the electric field/plasma motion and plasma density profiler instrument are all necessary.

The FUV imaging spectrometer with the appropriate limb observation method could obtain the neutral composition profiler and plasma density profiler by different spectral images in the FUV band (130–180 nm). It will help scientists to understand

how competing influences from above and below shape our space environment and concentrate its focus on middle and low latitudes to best capture the storm time variability of the ionosphere.

In this paper, we introduce a new prototype that is being developed in our program, the global atmospheric driver and ionosphere connection explorer (GADICON) FUV imaging spectrometer, operating in the FUV ranges to monitor the ionosphere. Besides the low mass and small volume of the compact instrument, it has excellent imaging and spectral resolved capabilities to retrieve O and N_2 spectral contents. The design principle, the parameters, and manufacturing of the instrument and laboratory calibration and tests are presented.

2. DESIGN PRINCIPLE FOR O AND N_2 LBH BANDS

A. Environmental Conditions, Design Rules, and Observation Method

The GADICON spectrometer is a limb-scanning instrument. It is designed for polar (inclination 98.75°) sun-synchronous mutually orthogonal orbit satellite and its –Z axis is always pointing toward and perpendicular to the surface of the Earth. Our designed instrument has a nadir line of sight that is parallel to this axis. Therefore, its nadir view ports are always directed to Earth. The orbit altitude of the equator is 836 km with a period 101.5 min. The instrument will work 14 periods in 24 h.

The operation of the instrument includes three main regimes: ionosphere observation (through the main window), dark calibration, and sun calibration (through the main window by the diffuser).

The ionosphere observation is the main operation. First, a global limb scanning imaging can be obtained in one day, which will be helpful for ionospheric inversion integrity and consistency. The limb scanning of the ionosphere profiler is the "lateral limb" scanning. When the one-day observation ends, it will apply two lateral limb imaging strips of the global ionosphere around the Earth, which will supply more information about the ionosphere.

The limb observations on two sides are defined in Fig. 1.

According to the sensitivity requirements (the relative analysis will be presented in the next part), the imaging integration time is defined as 22 s. The instrument monitors the ionosphere with an instantaneous field of view (FOV) of 6° × 0.046°. The direction of 6° is along the flying orbit and the direction of 0.046° is the scanning direction. The scanning will cover a vertical (FOV) at 17°, which will cover the limb altitude from 50 to 1000 km. The distance between the instrument and the observation point is about 3274.5 km. The total observation processing includes four steps. First, the instrument scans one limb side in 22 s. When the scanning ends, the scanning mirror will quickly rotate to the other limb side in 0.5 s. It also takes 22 s to complete this limb observation. When this scanning ends, the scanning mirror rotates to the initial location and the observation processing ends. The satellite has a flying speed of 7 km/s and passes 315 km in an observation period of 45 s. The spatial field-of-view covers a width of 341 km in the limb observation. It guarantees that the stripes in 14 orbits could cover the global ionosphere profiler.

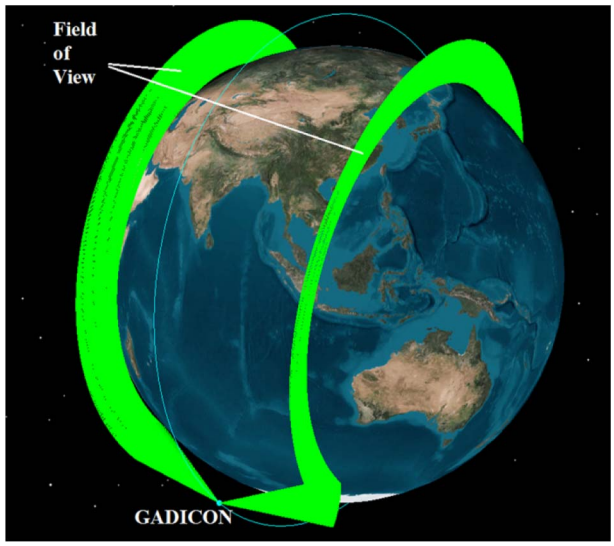

Fig. 1. Two imaging strips in the "two-sides" lateral limb observation.

The absence of a blackbody source being bright enough in the FUV makes it difficult to realize the high precision FUV calibration on orbit. However, in space one does have such sources as hot A and B dwarf stars. Their spectra are close to blackbody at most wavelengths, and are well characterized and stable in the FUV. Therefore, the stars could be the standard sources for our on-orbit calibration. The absolute radiance calibration can be operated once per month. The dark calibration includes dark current monitoring and wavelength calibration and can be operated once per day.

B. Observation Channels

To implement the new scientific requirements, the FUV instrument should measure the altitude distribution of the OI and N_2 dayglow emissions and the altitude and spatial distribution of the OI nightglow emissions. With these quantities, the important ionospheric information can be obtained in two observation modes.

In the dayside observation, photoelectrons colliding with atmospheric neutrals, N_2 and O, produce emissions, and by observing the limb brightness of the N_2 Lyman–Birge–Hopfield (LBH) bands 140–180 nm and of OI 135.6 nm, the density ratio of the neutral N_2 and O atmospheric constituents can be retrieved.

In the nightside observation, the recombination of O+ ions with ionospheric electrons also creates OI 135.6 nm emissions and the nighttime electron density can be estimated from the limb brightness of 135.6 nm.

With the above scientific requirements, the observation channel could be determined as 135.6 nm and 140–180 nm to cover the radiation of O+ and N_2 LBH bands.

3. SPECTROMETER DESIGN OF THE TWO CHANNELS

A. Specifications of the Imaging Spectrometer

The designed imaging spectrometer specifications for the two channels have been listed in Table 1.

Table 1. Summary of FUV Channel Specifications

Characteristic	Value or Range
Waveband	135.6 nm, 140–180 nm
Spectral resolution	≤0.6 nm
Pixel sampling (FWHM)	≥2
FOV	6° × 0.046°
Pixel spatial resolution	<0.5 mrad
Coverage of vertical height	50–1000 km
Projected counting rate	0.03 count/pix/exp/R
Integration time	22 s
Slit	10.5 mm × 0.08 mm
Entrance aperture diameter	20 mm
Focal length	100 mm
Mass (predicting)	12 kg
Dimensions (predicting)	380 mm × 300 mm × 200 mm

B. Characteristics of Detector and Responsivity Analysis

The detectors are the specific intensified FUV detector coupled to a microchannel plate (MCP). The pixel is 40 μm × 40 μm. The spectral dimension of the detector needs 524 pixels, and the spatial dimension needs 262 pixels.

The FUV detector characteristics are summarized in Table 2.

The detector is being studied by our Institute. With a standard detector from the NIST, it has been calibrated. The tested quantum efficiency (QE) of the detector is shown in Fig. 2.

An important parameter of the detector, the projected counting rate, which is also the responsivity of the detector, is not listed in Table 2. It is calculated by the following processing based on the system analysis. The radiance range of 135.6 nm in the ionosphere is about (100 Rayleigh, 10,000 Rayleigh). Rayleigh is the unit for light radiance, especially weak light [20]. The reference radiance is 5000 Rayleigh for the wavelength 135.6 nm. It is our design criterion for the responsivity of the detector. The transmission efficiency of our instrument could be expressed as

$$\tau = \frac{\pi}{4F^2} \times \epsilon, \tag{1}$$

where F is the F number of the optical system and ϵ is the total reflectance efficiency of all optical elements, which is 0.01 for our instrument. According to these conditions, the radiation transmitted by the imaging spectrometer achieved at the detector will be 1.57 Rayleigh. To make the detector have a count per pixel and per second under the radiation at least 1.57 Rayleigh, the projected counting rate should be 0.0289 count/pixel/s/R. Therefore, the rational responsivity of the detector should be larger than 0.03 count/pixel/s/R. Our detector is shown in Fig. 3.

Table 2. Characteristics of FUV Detector

Characteristic	Value
Effective receiving surface	30 mm diameter
Maximum count rate	>70 K counts/s
Input window	Magnesium fluoride
MCP arrangement	V stack (2 plates)
Photocathode	Cesium Iodide(MCP front surface)
QE	>10% in working waveband
Pixel	40 μm × 40 μm
High voltage power supply	Adjustable for variable gain

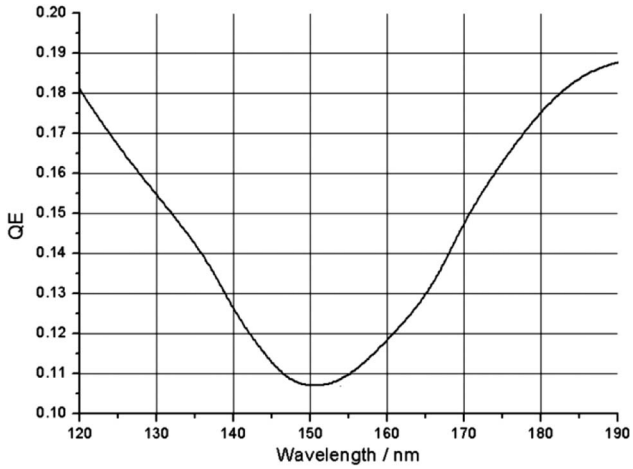

Fig. 2. QE of the detector.

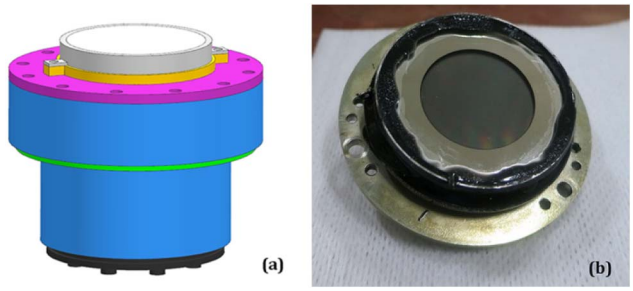

Fig. 3. (a) Sketch of the detector; (b) actual front part of detector.

C. Optical Design

With the above-mentioned design objectives and maximum maintenance of previous FUV load heritage as drivers, it was decided to build the imaging spectrometer around a plane grating system [21].

The optical layout of the FUV imaging spectrometer is shown in Fig. 4. The front-end optics consists of a scanning mirror (1), an entrance pupil (2), and an off-axis parabolic telescope (3) matching the incoming light beam. The slit (4) is placed in the image plane of the telescope to define the FOV

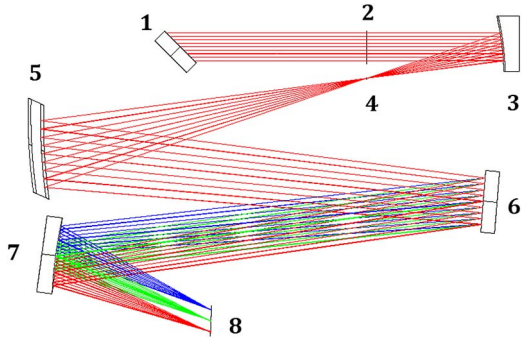

Fig. 4. Optical design layout in 2D.

of the system. The following part is the imaging spectrometer with high transmission efficiency. An elliptical reflecting mirror (5) serves as a collimating mirror and offers a parallel light beam to the plane grating (6). The dispersed beam is reflected by an oblate ellipsoid reflecting mirror (7), serving as an imaging lens, is projected on the detector (8).

The system is not an advanced Czerny–Turner system, strictly speaking. The reflectance light from the elliptical reflecting mirror (5) is not strict collimating light but with a little convergence. The arrangement of the elliptical reflecting mirror (5) and the oblate ellipsoid reflecting mirror (7) will help eliminate the astigmatism. The system is more effective for the high NA imaging spectrometer. The relative optical properties of system have been listed in Table 3.

The design results are shown in Fig. 5.

D. Spectral Resolution and Tolerance Analysis

According to Yu's study [22], the spectral resolution of the spectrometer could be expressed as

$$\Delta\lambda = \frac{\cos i}{mgf_1} b \cos \alpha, \tag{2}$$

where i is the incident angle of grating as 11° in our design, m is the 1st diffraction order, g is the rules density of grating, f_1 is the focal length of the collimating mirror, b is the width of the slit and α is the inclined angle of the imaging plane as 20.6°. Substituting these defined parameters into expression (2), the theoretic spectral resolution of the designed imaging spectrometer is calculated as 0.33 nm and satisfies the requirement.

The tolerance analysis of the designed system is simulated by the Monte Carlo method using ZEMAX software. The appropriate default tolerances of the system are listed in Table 4.

Using the wavelength 150 nm, the average geometric modulation transfer function (MTF) is calculated by the tolerances

Table 3. First-order Optical Properties

Parameter	Value
Overall focal length	100 mm
Entrance aperture (EA)	Φ 20 mm
Type of scanning mirror	Plane
Type of telescope	Off-axis parabolic
Radius of telescope	200 mm
Off-axis distance of telescope	30 mm
Distance between EA and telescope	100 mm
Size of slit	10.5 mm × 0.08 mm
Distance between telescope and slit	100 mm
Type of collimating mirror (CM)	
Conic of CM	−0.174
Radius of CM	376.97 mm
Distance between slit and CM	200 mm
Type of diffraction grating (DG)	Plane
Density of DG	1200 l/mm
Distance between CM and DG	350 mm
Type of focusing mirror (FM)	
Conic of FM	0.575
Radius of FM	340 mm
Distance between DG and FM	310.99 mm
Type of imaging plane (IP)	Plane
Distance between FM and IP	117.37 mm
Paraxial magnification	1×

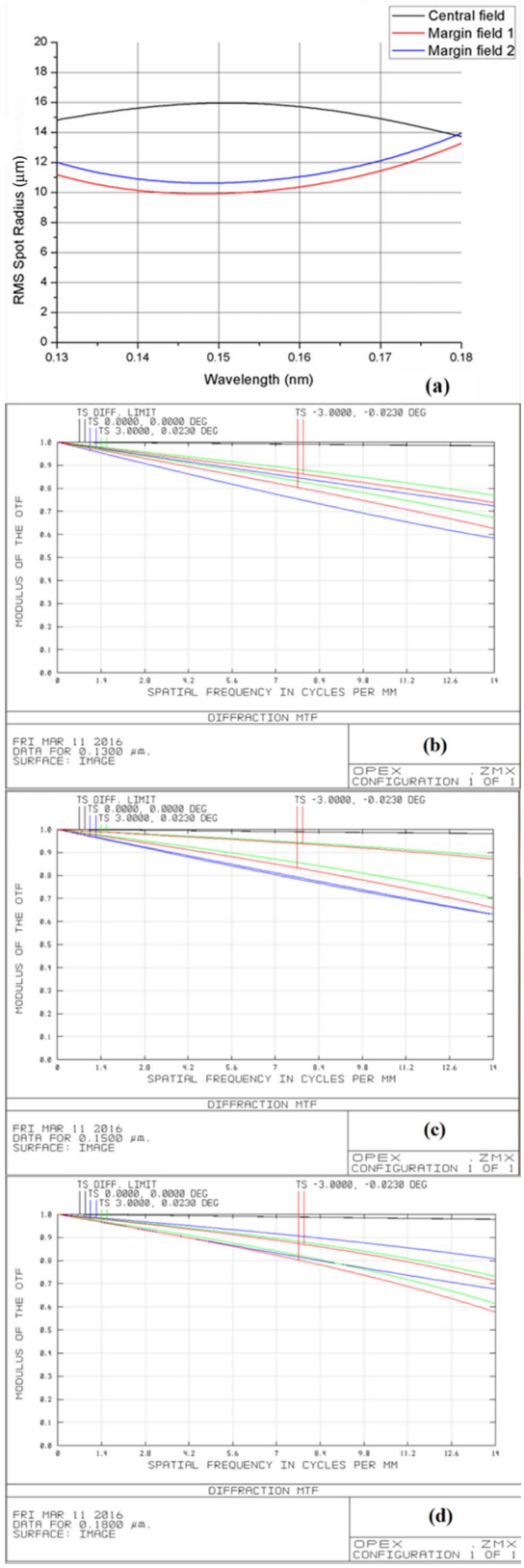

Fig. 5. Optical design results. (a) RMS spots radii versus wavelength; (b) MTF for 130 nm; (c) MTF for 150 nm; and (d) MTF for 180 nm.

Table 4. Default Tolerances Set

Surface Tolerances	
Radius	1 fringe
Thickness	0.2 mm
Tilt in X	0.02°
Tilt in Y	0.02°
Element Tolerances	
Decenter X	0.05 mm
Decenter Y	0.05 mm
Tilt X	0.02°
Tilt Y	0.02°

Table 5. Nine Worst Offenders

Type	Surface	Value	Criterion	MTF Change
TTHI	2, 3	0.1	0.56468671	−0.02965995
TTHI	7, 8	−0.1	0.56822912	−0.02611753
TETX	8, 8	0.02	0.57814887	−0.01619778
TFRN	11	−2	0.58345131	−0.01089534
TETY	8, 8	0.02	0.58682039	−0.00752627
TTHI	10, 11	0.1	0.58805876	−0.00628789
TEDY	8, 8	0.05	0.58830448	−0.00604217
TTHI	13, 14	−0.1	0.58869739	−0.00564926
TETY	11, 11	−0.02	0.59019712	−0.00414953
TFRN	14	−2	0.59111031	−0.00323635

ranges. Nine kinds of tolerances of the system which influence the design results most are listed in Table 5.

It can be seen that the tolerances of the distance between surfaces 2 and 3 and the distance between surfaces 7 and 8, and the tilt of element 8 influences the design results of the optical system. The statistical results have been obtained including 20 trials and normal distribution. We present three results under three different wavelengths as 130, 150, and 180 nm.

(1) 130 nm. In the statistical results, 90% of the MTF of the system are greater than 0.49346783, 50% of the MTF of the system are greater than 0.52621566 and 10% of the MTF of the system are greater than 0.54016274.

(2) 150 nm. In the statistical results, 90% of the MTF of the system are greater than 0.50962837, 50% of the MTF of the system are greater than 0.53860026 and 10% of the MTF of the system are greater than 0.54766820.

(3) 180 nm. In the statistical results, 90% of the MTF of the system are greater than 0.49550265, 50% of the MTF of the system are greater than 0.53417321 and 10% of the MTF of the system are greater than 0.54693109.

The previous calculated results demonstrate that the tolerances of the total optical system are rational.

E. Optical Elements and Mechanics of Prototype

The optical elements of the prototype include plane grating (1), an off-axis parabolic mirror (2), a collimating mirror (3) and a focusing mirror (4), as in Fig. 6.

The RMS of the mirrors' surface flatness is about $\lambda/50$ ($\lambda = 632.8$ nm). The FUV grating is introduced from the company JY. The optical reflectance layers on the mirrors

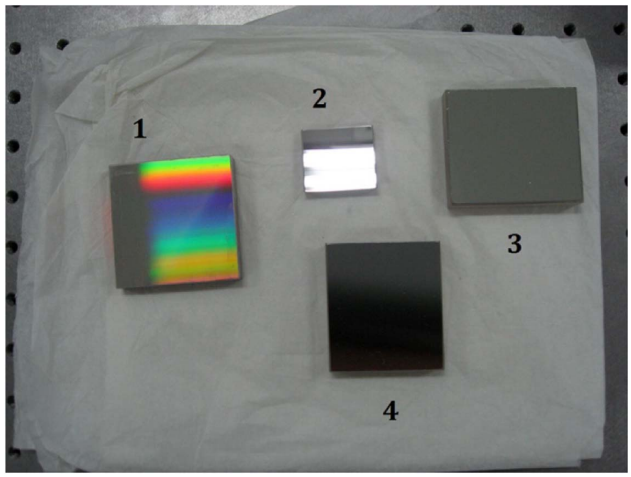

Fig. 6. Optical elements of the prototype.

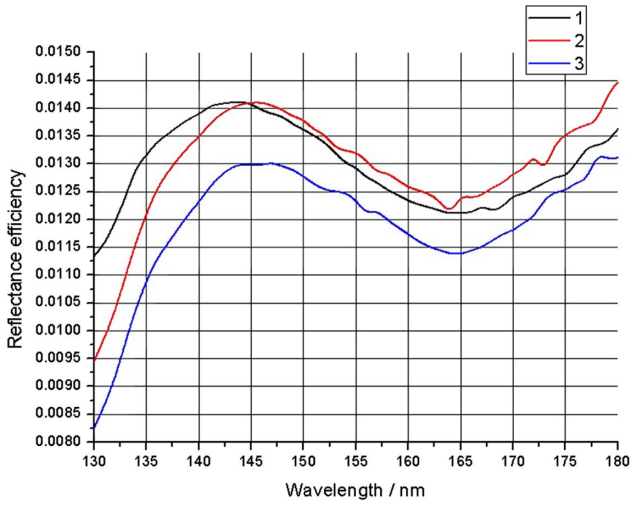

Fig. 7. Total reflectance efficiency.

are aluminum and MgF2. The total reflectance efficiencies of the prototype are expressed as curves in Fig. 7.

The fitted curve 1 in Fig. 7 is the transmission efficiency of the optical system when the spectrometer is aligned. Curve 2 was obtained two months later. Curve 3 was obtained four months later. The total reflectance efficiency exhibits hardly any variation.

The mechanism of the prototype is presented in Fig. 8. The prototype includes the scanning mirror (1), the entrance pupil (2), the slit (3), the telescope (4), the collimating mirror (5), the focusing mirror (6), the plane grating (7), the detector (8) and the mechanical shell.

4. LABORATORY GROUND PERFORMANCE TESTS AND CALIBRATION

A. Irradiation Calibration

For FUV calibration, the elements such as light source, vacuum environment, and calibration time will introduce more errors

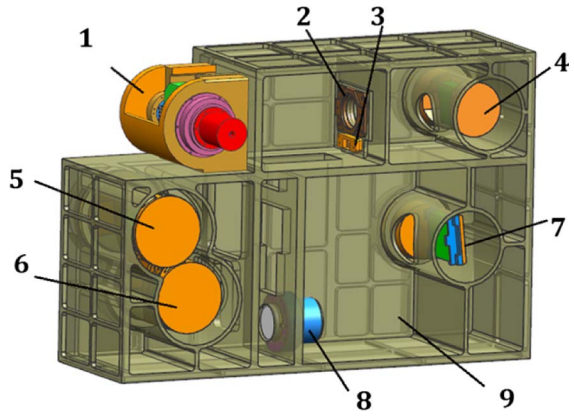

Fig. 8. Mechanism of the prototype.

than in the other wavebands' calibration. The absence of a calibrated source and calibrated black body in FUV make it more difficult to obtain a precise calibration, especially for radiation calibration [23]. Therefore, absolute irradiation calibration is adopted.

First, the calibrated illumination system is built. The deuterium lamp V03 from the company Cathoden is used. The working voltage is 70 V, the working current is 300 mA, and the power is 30 W. Its stability could be 0.03% per hour. The deuterium lamp could be considered as a point source. A collimating system is introduced to make the light become the parallel light. For the convenience of wavelength changing, a Czerny–Turner vacuum ultraviolet monochromator is added between the lamp and the collimator. When this illumination source system was built, a calibrated detector was used to calibrate it. The system is shown in Fig. 9.

The uniformity of the calibrated illumination system is better than 0.2% by the test. A calibrated detector has been used to calibrate the system. The calibrated detector owns a standard QE data curve. The relationship of the QE and readout value $D(\lambda)$ could be expressed as

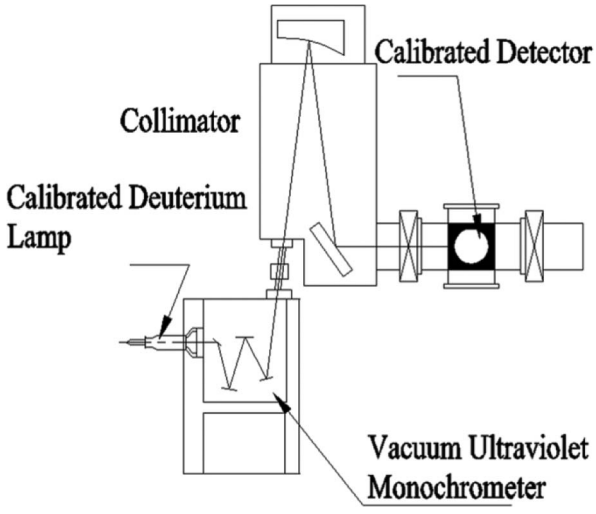

Fig. 9. Sketch of FUV-calibrated illumination system.

$$\mathrm{QE}(\lambda) = \frac{h \cdot c \cdot D(\lambda)}{n \cdot e \cdot \phi(\lambda)}, \tag{3}$$

where h is the Planck constant, c is the light velocity, and $\phi(\lambda)$ is the light flux received by the detector. With these conditions, the expression (3) could be changed to

$$\mathrm{QE}(\lambda) = 1239.85 \cdot \frac{D(\lambda)}{\phi(\lambda)} = 1239.85 \cdot I(\lambda), \tag{4}$$

where $I(\lambda)$ is the spectral responsibility of the detector with the unit as V/W or A/W. The calibrated spectral irradiation $E(\lambda)$ of the front light system is expressed as

$$E(\lambda) = \frac{\phi(\lambda)}{S} = 1239.85 \cdot \frac{D(\lambda)}{\pi r^2 \cdot EQS(\lambda)}, \tag{5}$$

where $S = \pi r^2$ is the area of the collimating light. At this time, the calibrated illumination source system has been built. The calibrated spectral irradiation of the unit has also been obtained.

The total experimental system for the prototype irradiation calibration is shown in Fig. 10. The prototype instrument and a calibrated detector have been arranged on a precision turntable. The precision turntable could keep the locations of the prototype and the detector. These mountings are put into the vacuum system. The calibrated illumination system is arranged in front of the vacuum system. The distance between it and the prototype is 1 m.

The actual experimental mounting for the prototype calibration is shown in Fig. 11.

According to the analysis, the spectral irradiance responsibility of the prototype is expressed as

$$R(\lambda) = \frac{E(\lambda)}{D'(\lambda)} = 1239.85 \cdot \frac{D(\lambda)}{\pi r^2 \cdot EQS(\lambda) \cdot D'(\lambda)}, \tag{6}$$

where $D'(\lambda)$ is the readout value of the prototype. The spectral irradiance responsibility curve of the prototype has been presented in Fig. 12.

B. Spectral Resolution

A McPherson monochromator which works in the waveband 115–400 nm with the spectral resolution 0.01 nm has been adopted to test the spectral resolution of the imaging spectrometer prototype. The detecting wavelength is chosen as 171 nm. The result is presented in Fig. 13.

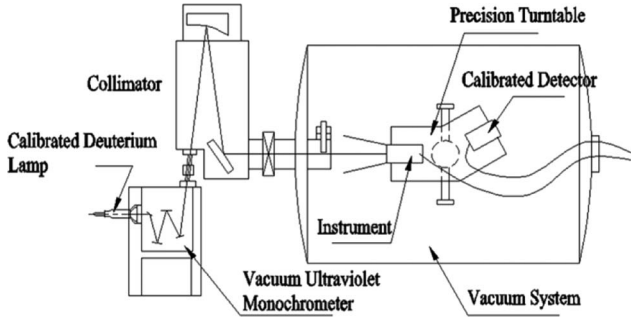

Fig. 10. Experimental mounting for the prototype irradiation calibration.

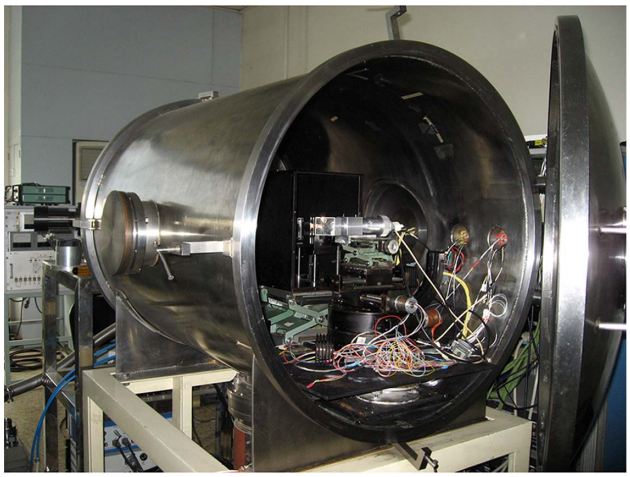

Fig. 11. Actual experimental mounting.

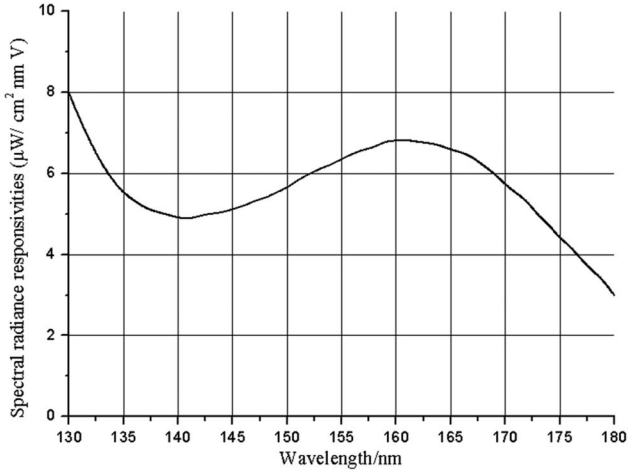

Fig. 12. Spectral irradiation responsibility of the prototype.

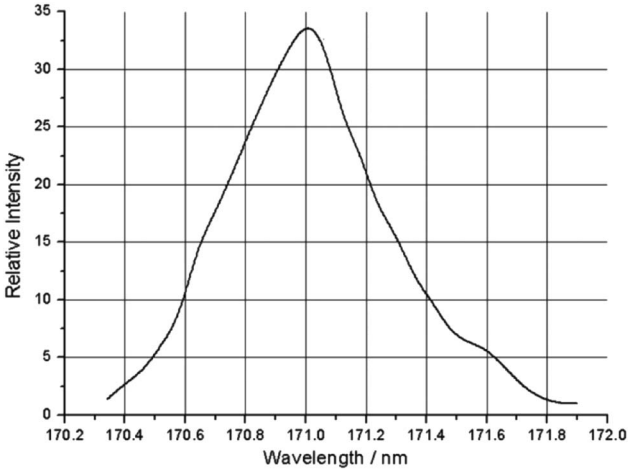

Fig. 13. Shape of the detecting wavelength: 171 nm.

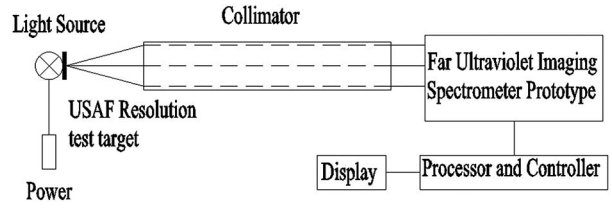

Fig. 14. Sketch of the spatial resolution detecting system.

The x-coordinate is the wavelength with the unit as nm. The y-coordinate is the monitored spectral relative intensity. According to the data, the FWHM of the wave shape, which is also the spectral resolution, is 0.57 nm. It satisfies the scientific requirement but is lower than the theoretical value. The error mainly comes from the manufacture and the alignment of the prototype.

C. Spatial Resolution

The spatial resolution of the prototype is tested by the detecting system in Fig. 14.

The light source is the deuterium lamp which covers the FUV waveband. The lamp will illuminate the United States Air Force (USAF) resolution test target, and the imaging of USAF resolution test target will pass the collimator to reach the prototype. By analysis of the imaging, the spatial resolution of the prototype will be obtained. The imaging of the USAF resolution test target in FUV test is shown in Fig. 15.

The best part of imaging of the USAF resolution test target is shown in Fig. 16.

The format of N_c expresses the resolved spatial frequency as

$$N_c = 2^{(k+\frac{m-1}{6})}, \tag{7}$$

where k and m are the vertical and horizontal numbers in the USAF resolution test target. The maximum resolved spatial resolution imaging is obtained by the data analysis. The corresponding part of imaging data is presented in Fig. 17. It should be known that the prototype can distinguish the spatial frequency $k = 2$, $m = 3$. According to the format (7), the resolved spatial frequency N_c is 5.04 lp/mm. The focal length of the collimator is 220 mm, and the focal length of the

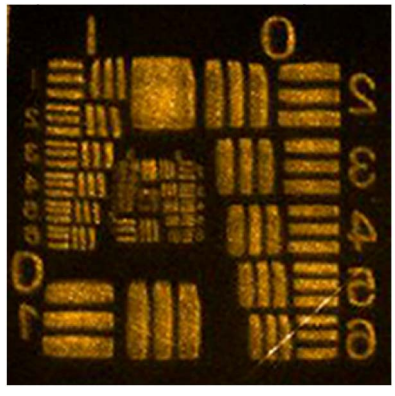

Fig. 15. USAF resolution test target.

Fig. 16. Imaging of the USAF resolution test target of the prototype.

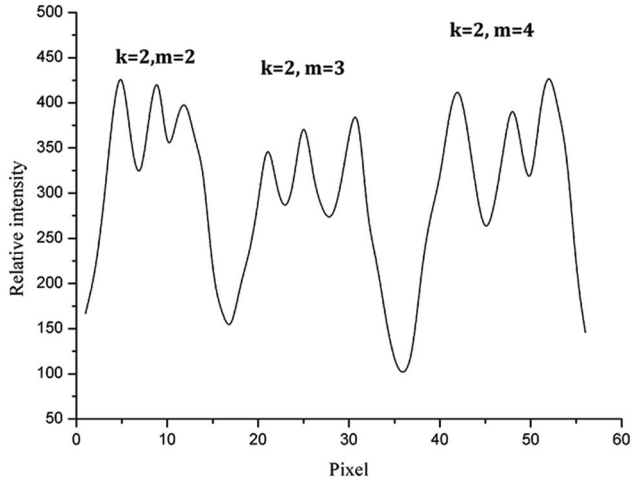

Fig. 17. Intensity profiles of imaging of the USAF resolution test target.

prototype is 100 mm. Therefore, the spatial resolution of the prototype is calculated as

$$N = N_c f_c / f = 11.1 \text{ lp/mm}. \quad (8)$$

The equivalent spatial resolution is 0.45 mrad. It is still lower than the theoretical design parameter. The error also comes from the manufacture and the alignment of the prototype. However, it can satisfy the scientific requirement.

5. CONCLUSION

In conclusion, the paper has described the design and testing of the FUV imaging spectrometer prototype for ionosphere observation. Our research will offer an occasion to achieve the scientific goal to study the forces acting from below which strongly influence the ionosphere. The design, the manufacturing, and the laboratory tests and calibrations have been completed in our work. The observation channels of the imaging spectrometer prototype, which are described within this paper, will offer good spectral resolution (0.57 nm) and spatial resolution (0.45 mrad), appropriate observation (two sided lateral limb observation), and excellent sensitivity (0.03 count/pix/exp/R) during 135.6 nm, 140–180 nm.

Funding. National Natural Science Foundation of China (NSFC) (41504143); Youth Innovation Promotion Association of the Chinese Academy of Sciences (2016203).

REFERENCES

1. R. R. Meier, "Ultraviolet spectroscopy and remote sensing of the upper atmosphere," Space Sci. Rev. **58**, 1–185 (1991).
2. R. P. McCoy, "Space weather comes of age: new sensors and models for ionospheric specification and forecast," Proc. SPIE **5548**, 341–347 (2004).
3. F. W. Schenkel, B. S. Ogorzalek, J. C. Larrabee, F. J. LeBlanc, and R. E. Huffman, "Ultraviolet daytime auroral and ionospheric imaging from space," Appl. Opt. **24**, 3395–3405 (1985).
4. D. A. Elliott, T. S. Pagano, and H. H. Aumann, "The impact of the AIRS spatial response on channel-to-channel and multi-instrument data analyses," Proc. SPIE **6296**, 62960I (2006).
5. K. F. Dymond and R. P. McCoy, "Ultraviolet spectrographs for thermospheric and ionospheric remote sensing," Proc. SPIE **1940**, 117–127 (1993).
6. R. P. McCoy, K. F. Dymond, G. G. Fritz, S. E. Thonnard, R. R. Meier, and P. A. Regeon, "Special sensor ultraviolet limb imager: an ionospheric and neutral density profiler for the defense meteorological satellite program satellites," Opt. Eng. **33**, 423–429 (1994).
7. L. J. Paxton, C.-I. Meng, G. H. Fountain, B. S. Ogorzalek, E. H. Darlington, S. A. Gary, J. O. Goldsten, D. Y. Kusnierkiewicz, S. C. Lee, L. A. Linstrom, J. J. Maynard, K. Peacck, D. F. Persons, and B. E. Smith, "SSUSI: horizon to horizon and limb-viewing spectrographic imager for remote sensing of environmental parameters," Proc. SPIE **1764**, 161–176 (1992).
8. A. B. Christensen, D. C. Kayser, J. B. Pranke, P. R. Straus, D. G. Gutierrez, S. Chakrabarti, R. P. McCoy, R. R. Meier, K. D. Wolfram, and J. M. Picone, "Instrumentation on the remote atmospheric and ionospheric detection system experiment; extreme-ultraviolet spectrometer, photometer, and near-infrared spectrometer," Opt. Eng. **32**, 3054–3059 (1993).
9. L. J. Paxton, A. B. Christensen, D. Morrison, B. Wolven, H. Kil, Y. Zhang, B. S. Ogorzalek, D. C. Humm, J. Goldsten, R. DeMajistre, and C.-I. Meng, "GUVI: a hyperspectral imager for geospace," Proc. SPIE **5660**, 228–239 (2004).
10. L. J. Paxton, A. B. Christensen, D. C. Humm, B. S. Ogorzalek, C. T. Pardoe, D. Morrison, M. B. Weiss, W. Crain, P. H. Lew, D. J. Mabry, J. O. Goldsten, S. A. Gary, D. F. Persons, M. J. Harold, E. B. Alvarez, C. J. Ercol, D. J. Strickland, and C.-I. Meng, "Global ultraviolet imager (GUVI): measuring composition and energy inputs for the NASA thermosphere ionosphere mesosphere energetics and dynamics (TIMED) mission," Proc. SPIE **3756**, 265–276 (1999).
11. E. R. Talaat, J.-H. Yee, S.-Y. Hsieh, L. J. Paxton, R. DeMajistre, A. B. Christensen, and D. Bilitza, "The quiet nighttime low-latitude ionosphere as observed by TIMED/GUVI," Adv. Space Res. **51**, 661–676 (2013).
12. D. M. Riggin, H.-L. Liu, R. S. Lieberman, R. G. Roble, J. M. Russell, C. J. Mertens, M. G. Mlynczak, D. Pancheva, S. J. Franke, Y. Murayama, A. H. Manson, C. E. Meek, and R. A. Vincent, "Observations of the 5-day wave in the mesosphere and lower thermosphere," J. Atmos. Solar-Terr. Phys. **68**, 323–339 (2006).
13. A. Aksnes, R. Eastes, S. Budzien, and K. Dymond, "Neutral temperatures in the lower thermosphere from N_2 Lyman-Birge-Hopfield (LBH) band profiles," Geophys. Res. Lett. **33**, L15103 (2006).
14. J. R. Souza, W. D. Asevedo, P. C. P. dos Santos, A. Petry, G. J. Bailey, I. S. Batista, and M. A. Abdu, "Longitudinal variation of the equatorial ionosphere: modeling and experimental results," Adv. Space Res. **51**, 654–660 (2013).
15. Y.-I. Zhang, L. J. Paxton, and H. Kil, "Nightside midlatitude ionospheric arcs: TIMED/GUVI observations," J. Geophys. Res. **118**, 3584–3591 (2013).

16. T. Sotirelis, H. Korth, S.-Y. Hsieh, Y.-L. Zhang, D. Morrison, and L. Paxton, "Empirical relationship between electron precipitation and far-ultraviolet auroral emissions from DMSP observations," J. Geophys. Res. **118**, 1203–1209 (2013).
17. H. Kil, W. K. Lee, J. Shim, L. J. Paxton, and Y. Zhang, "The effect of the 135.6 nm emission originated from the ionosphere on the TIMED/GUVI O/N_2 ratio," J. Geophys. Res. **118**, 859–865 (2013).
18. R. W. Eastes, D. J. Murray, A. Aksnes, S. A. Budzien, R. E. Daniell, and A. Krywonos, "Modeled and observed N_2 Lyman-Birge-Hopfield band emissions: a comparison," J. Geophys. Res. **116**, A12308 (2011).
19. A. B. Christensen, L. J. Paxton, S. Avery, J. Craven, G. Crowley, D. C. Humm, H. Kil, R. R. Meier, C.-I. Meng, D. Morrison, B. S. Ogorzalek, P. Straus, D. J. Strickland, R. M. Swenson, R. L. Walterscheid, and B. Wolven, "Initial observations with the global ultraviolet imager (GUVI) in the NASA TIMED satellite mission," J. Geophys. Res. **108**, 1451 (2003).
20. D. J. Baker, "Rayleigh, the unit for light radiance," Appl. Opt. **13**, 2160–2163 (1974).
21. M. Futamata, T. Takenouchi, and K. I. Katakura, "Highly efficient and aberration-corrected spectrometer for advanced Raman spectroscopy," Appl. Opt. **41**, 4655–4665 (2002).
22. L. Yu, S.-R. Wang, Y. Qu, and G.-Y. Lin, "Broadband FUV imaging spectrometer: advanced design with a single toroidal uniform-line-space grating," Appl. Opt. **50**, 4468–4477 (2011).
23. B. S. Dandekar and D. J. Davis, Jr., "Calibrations of the airglow photometers and spectrometers," Appl. Opt. **12**, 825–831 (1973).